Korean J. Chem. Eng., 39(10), 2623-2635 (2022)
DOI: 10.1007/s11814-022-1191-3

pISSN: 0256-1115
eISSN: 1975-7220

Analysis of the extrusion pressure of a cylindrical extruder for extruding highly viscous fluids

Zhibin Sun*,, Baojun Shen*,**, Yu He*,**, Jiecai Long*,**, Xiaobin Zhan*,**, Yujin Li*,**, and Xiwen Li*,**,†**

*State Key Laboratory of Digital Manufacturing Equipment and Technology, Huazhong University of Science and Technology, Wuhan 430074, China
**School of Mechanical Science and Engineering, Huazhong University of Science and Technology, Wuhan 430074, China
(*Received 16 December 2021 • Revised 15 April 2022 • Accepted 26 May 2022*)

Abstract−Extrusion pressure is crucial for the security and performance of a cylindrical extruder during the extrusion process. In this study, a validated CFD model was adopted to evaluate the relationship between the extrusion velocity, fluid viscosity, and the extrusion pressure of a cylindrical extruder while extruding highly viscous fluids. The simulated and experimental results of the extrusion pressure and velocity profiles show good agreement. This study reveals that extrusion pressure evolution can be divided into two stages during the extrusion process. At stage I, the distance between the ram and the bottom of the vessel (liquid height) is greater than the critical height and the extrusion pressure remains almost constant. At stage II, the distance is less than the critical height and the extrusion pressure increases exponentially. The results indicate that an increase in extrusion velocity and fluid viscosity leads to a linear increase in the extrusion pressure at stage I. Furthermore, by introducing a pressure number, N_p, and a pressure-related Reynolds number, Re_p, a novel correlation of the extrusion pressure with the extrusion velocity, viscosity of highly viscous fluids and liquid height has been developed.

Keywords: Cylindrical Extruder, Extrusion Pressure, Critical Height, CFD, Highly Viscous Fluids

INTRODUCTION

In the chemical industry, it is necessary to transfer highly viscous fluids between containers in different processes, such as transferring homogeneously mixed slurries in the mixing vessel to the storage tank. However, pouring highly viscous fluids from one vessel into another is inefficient due to its poor fluidity. Cylindrical extruders are widely used in food processing, ceramics and 3D printing to drive the highly viscous material out of the vessel [1-6]. A cylindrical extruder can propel fluids of any viscosity out of the vessel at a predetermined rate based on requirements [7,8]. Using cylindrical extruders to drive fluids is more efficient than the traditional method of turning over the vessel to pour out the fluid, and this method results in less fluid residue in the vessel. To the best of our knowledge, no previous investigation on evaluating the internal flow field characteristics during the extrusion process has been carried out on the cylindrical extruder. Due to the lack of understanding of extrusion mechanisms and fluid transport phenomena, it is difficult to determine cylindrical extruders' operating parameters accurately.

To reveal the extrusion mechanism of a cylindrical extruder while extruding highly viscous fluids, it is necessary to understand the complex flow field deeply. As a non-invasive measurement technique, particle image velocity (PIV) can provide velocity data at high spatial resolution, which has been widely used to measure the velocity fields and velocity distribution [9-11]. In addition to PIV experimental studies, computational fluid dynamics (CFD) is a powerful tool for investigating the flow features [12-15]. Through CFD simulation, Jay et al. [16] examined the effects of yield stress and pressure loss when viscoplastic fluid flowed through axisymmetric contractions, and proposed a map for predicting the flow structure. Liu et al. [17] numerically investigated the pressure distribution and velocity of materials during extrusion, and explored the effects of rheological parameters of materials on the extrusion state. Previous studies have shown that the CFD method can simulate the distribution of velocity and pressure during the extrusion process. PIV experiments are time-consuming and expensive, it is difficult or even impossible for PIV to obtain results from studies involving many parameters [18]. Therefore, experimental (such as PIV) and numerical investigations need to be conducted concurrently to obtain the evolution of the flow field with the movement of the ram.

Furthermore, extrusion pressure is an important indicator that can affect working fluid properties and evaluate the safety of the extrusion process [19-23]. Therefore, it is necessary to predict the extrusion pressure and control it within an appropriate range. However, the current approach to predict the extrusion pressure is quite complicated for a fixed cylindrical extruder. Benbow et al. [24] proposed a model to calculate the extrusion pressure of cylindrical extruders:

$$P_{ex} = 2(\sigma_0 + \alpha v_{die}^m)\ln\frac{D}{d} + 4(\tau_0 + \beta v_{die}^n)\frac{L}{d} \quad (1)$$

where P_{ex} is the extrusion pressure (area-averaged pressure of the

†To whom correspondence should be addressed.
E-mail: xiwenli@hust.edu.cn

ram), v_{die} is the mean fluid velocity in the die land, D is the vessel diameter, d is the diameter of die land and L is the die land length. α and β are the velocity multiplier parameters, m and n are the velocity exponents, σ_0 is the yield stress, and τ_0 is the wall stress. The parameters α, β, m, and n are velocity-dependent. This model has multiple velocity-related factors that make it difficult to obtain specific values in practical applications, rather than the rheological parameters of fluids [3]. Furthermore, with Eq. (1), the yield stress σ_0 can be overestimated by about 20% to predict the extrusion pressure [19]. To reduce the fitting parameters and simplify the calculation process of predicting the extrusion pressure, Basterfield et al. [7] developed an analytical model of orifice extrusion that incorporates only the rheological parameters of fluids. However, as this model does not consider the pressure drop generated in the die land, its applicability is limited. Currently, the direct connection of the extrusion pressure of a cylindrical extruder with extrusion velocity and viscosity is not available.

This study investigated the extrusion performance of a cylindrical extruder while extruding highly viscous fluids. The extrusion pressure with different extrusion velocities was measured experimentally and compared with the CFD results. Besides, the velocity profiles obtained from CFD agree well with PIV experiment results, which validates the reliability of the CFD model. Then, the extrusion pressure evolution was analyzed to investigate the mechanism of the extrusion pressure variation. Subsequently, the effects of extrusion velocity and viscosity of fluids on the extrusion pressure were investigated. Finally, based on the CFD results, a distinct correlation of the extrusion pressure P_{ex} in terms of extrusion velocity v_{ram}, fluid viscosity μ and liquid height H was established by introducing a pressure number N_p and a pressure-related Reynolds number Re_p.

EXPERIMENTAL SETUP AND METHODS

1. The Extrusion Configuration and Material

An experimental setup was designed to validate the CFD model. Fig. 1 displays a schematic diagram of the experimental setup. The motor drives the ram to move downwards by driving the spiral elevator to perform extrusion, and this drives the fluid in the vessel to flow out through the die land at the bottom. The employed configuration has a vessel with a diameter of D=160 mm, a die land with a diameter of d=10 mm, and a length of L=60 mm. During the experiment, the fluids in the vessel had the same initial height of 70 mm, which means that the maximum distance H between the ram and the bottom of the vessel was 70 mm. The relevant geometric dimensions of the employed configuration are listed in Table 1.

The verification experiments consisted of a pressure experiment and a velocity field experiment. In the pressure experiment, the pressure sensor was mounted on the ram and located at a distance of 55 mm from the center of the ram, as illustrated in Fig. 2. The extrusion velocities (the velocity of ram movement) were set to 2 mm/s, 3 mm/s and 4 mm/s, respectively. During the movement of the ram from H=70 mm to H=5 mm, the pressure value was recorded every 5 mm of movement. All experiments were conducted thrice.

In the velocity field experiment, the velocity fields of fluids in the vessel were recorded by a 2D-PIV system (LaVision, Germany),

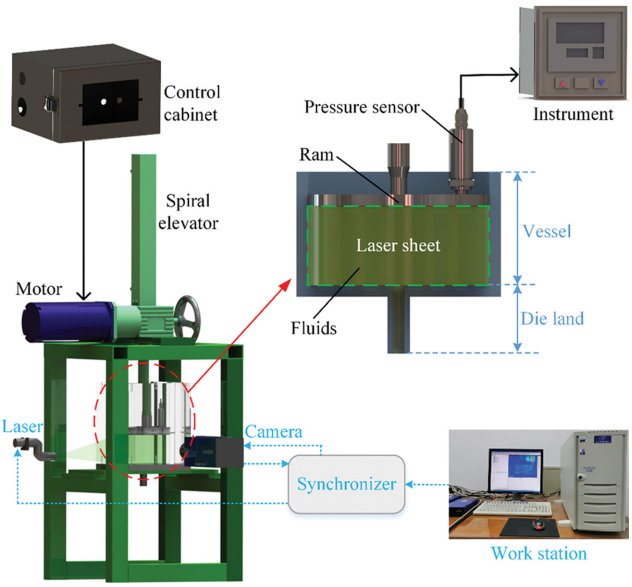

Fig. 1. Schematic diagram of the experimental setup.

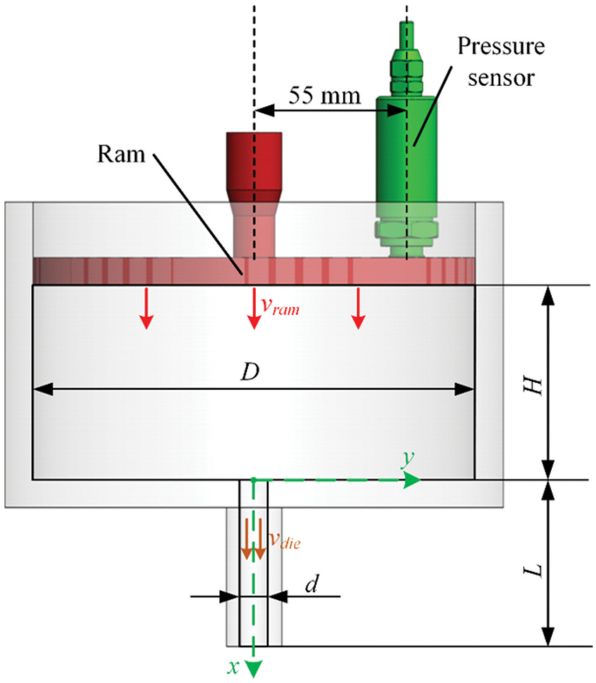

Fig. 2. Structural diagram of the vessel and die land.

which consists of a CCD camera (LaVision Imager Pro X 2M, 1600×1200 pixels^2, 7.4 μm in pixel pitch), a double-pulsed Nd:YAG laser (wavelength λ=532 nm, 200 mJ/pulse, 15 Hz, Litron, England) and a workstation, as shown in Fig. 1. To photograph the velocity fields inside the vessel, the vessel is made of transparent plexiglass (PMMA). Hollow glass spheres (9-13 mm in diameter and 1,100 kg/m^3 in density) were used as tracer particles and uniformly dispersed in the working fluid. LaVision Davis 7.2 software was used to process and analyze PIV images, and reliable time-averaged flow field from 20 pairs of particle images using the cross-correlation algorithm.

In this study, the experimental fluid chosen was corn syrup. Corn

Table 1. Geometric parameters of the employed configuration

Geometric parameters	Values
Diameter of the vessel, D	160 mm
Diameter of the die land, d	10 mm
Length of the die land, L	60 mm
Distance between ram and bottom of the vessel, H	0-70 mm

Table 2. Properties of the corn syrup

Fluid type	Density ρ (kg m^{-3})	Viscosity μ (Pa·s)
Newtonian	1,380	4

syrup is a Newtonian fluid. Table 2 shows its density and viscosity. The experiment was carried out at an ambient temperature of 23 °C.

In this study, the fluid used is incompressible. According to the conservation of mass, the relationship between the ram velocity v_{ram} and the average velocity of fluids in the die land v_{die} can be obtained from the relation, $v_{die}d^2=v_{ram}D^2$, or

$$v_{die}=v_{ram}\left(\frac{D^2}{d^2}\right) \tag{2}$$

2. Dimensional Analysis

Dimensional analysis is widely used in the study of fluid flow characteristics in various equipment, which aids in understanding the relationship between various flow process parameters [25-28].

Considering the geometric parameters of the equipment and the fluid properties in this study, the relevant parameters that affect the extrusion pressure of the cylindrical extruder include: [7,8,29]

$$P_{ex}=f_1(\mu, \rho, v_{ram}, D, d, L) \tag{3}$$

For a fixed extruder, the structural parameters of D, d and L are constants. Therefore, Eq. (3) can be simplified to:

$$P_{ex}=f_2(\mu, \rho, v_{ram}) \tag{4}$$

Two dimensionless parameters are defined considering the extrusion pressure of the ram during extrusion, P_{ex}, as the target variable: the pressure number N_p and the pressure-related Reynolds number Re_p. Thus, the solution process of P_{ex} can be simplified to:

$$P_{ex}=f_3(N_p) \tag{5}$$

$$N_p=f_4(Re_p) \tag{6}$$

in which:

$$N_p=\frac{P_{ex}}{\rho v_{die}^2} \tag{7}$$

$$Re_p=\frac{\rho v_{die} d}{\mu} \tag{8}$$

where P_{ex} denotes the extrusion pressure of the ram, in Pa, ρ is the density of the fluid, in kg/m^3, v_{die} is the average velocity of the fluid in the die land, in mm/s, d is the diameter of the die land, in mm.

According to Eq. (2), Eq. (7) and Eq. (8) can be re-written to get a direct correlation with the operating parameters of the extruder. The modified equations are:

$$N_p=\frac{P_{ex}d^4}{\rho v_{ram}^2 D^4} \tag{9}$$

$$Re_p=\frac{\rho v_{ram} D^2}{\mu d} \tag{10}$$

where v_{ram} is the extrusion velocity of the ram, in mm/s, D is the diameter of the vessel, in mm.

To summarize, the values of N_p and Re_p for a fixed extruder are dependent only on the extrusion velocity of the ram and the viscosity of the liquid.

CFD MODEL

The commercial CFD program ANSYS Fluent 19.0 was used to investigate the extrusion pressure changes. This CFD model numerically simulates the process of using a cylindrical extruder to drive fluids of various viscosities out of the extruder at different extrusion velocities.

In this study, the extrusion velocity v_{ram} of the ram and the viscosity μ of the fluid varied from 2 to 10 mm/s and from 4 to 20 Pa s, respectively. According to Ryltseva et al. [30], the Reynolds number in this research ranges 0.353 to 8.832. Therefore, during the extrusion process, the fluid flow in the extruder is assumed to be laminar, and the laminar model is used in the numerical procedure. For the steady-state flow, the conservation equations of continuity and momentum that describe the flow in the calculation domain are given as: [31]

$$\text{Continuity: } \rho\nabla\cdot\vec{v}=0 \tag{11}$$

$$\text{Momentum: } \rho\frac{\partial\vec{v}}{\partial t}+\rho\vec{v}\cdot\nabla\vec{v}=-\nabla p+\mu\nabla^2\vec{v}+\rho\vec{g}+\vec{F} \tag{12}$$

where $\vec{v}$ is the velocity vector, t is the time, p is the fluid pressure, $\vec{g}$ is the gravitational acceleration and $\vec{F}$ accounts for external body forces other than pressure, gravity and viscosity.

To improve calculation efficiency, a two-dimensional (2D) axisymmetric model and fluid dynamic model were combined to study the extrusion process. In the mesh model (see Fig. 3), the zone of the wall of the vessel is specified as stationary. The zone of the ram is specified as a moving rigid wall with no-slip boundary condition so that its velocity is defined by UDF. The dynamic mesh

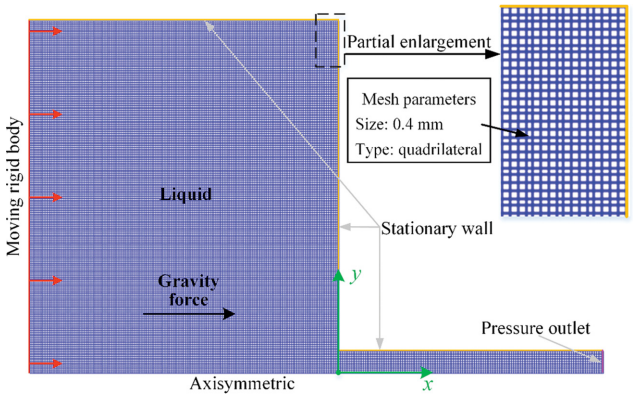

Fig. 3. Schematic diagram of computational domain with meshes.

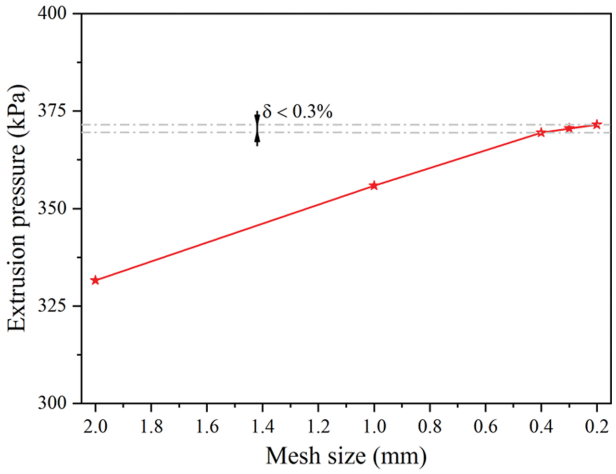

Fig. 4. Mesh dependency for the CFD model with v_{ram}=6 mm/s and μ=12 Pa s.

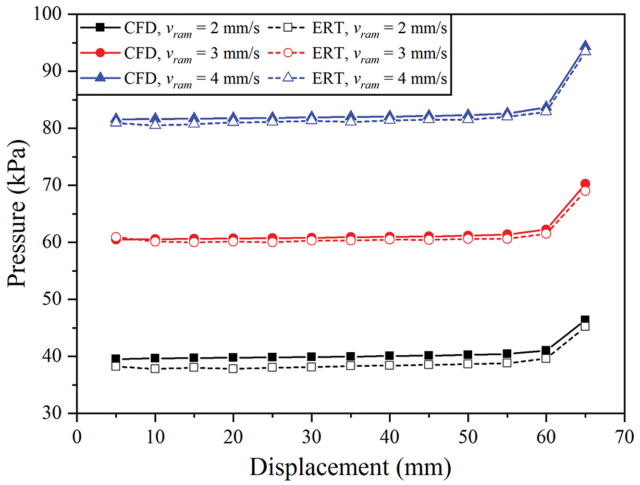

Fig. 5. Comparison of simulation (CFD) and experimental (ERT) values of pressure.

approach is applied to the moving wall of the numerical model. In this study, the movement of the ram and the hydrostatic pressure gradient were the driving forces that drive the flow through a cylindrical extruder. The cylindrical extruder outlet was set as pressure-outlet boundary with a static pressure equal to atmospheric pressure. The atmospheric pressure (101,325 Pa) was set as the operating pressure. The no-slip boundary conditions were adopted for the wall [32].

In all simulations, the pressure-velocity coupling was performed with the SIMPLEC algorithm. The least squares cell based method was used for the spatial discretization of the gradient term. The PRESTO! scheme was used for pressure interpolation. The momentum equations were solved by the QUICK scheme. The atmospheric pressure (101,325 Pa) was set as the operating pressure. The appropriate time step Δt, for the temporal resolution, was set at 0.001 s [33].

Fig. 3 illustrates the mesh model. Considering the axisymmetric characteristics of the model in this study, ICEM CFD 19.0 was used to generate the structured grids of the extruder fluid domain.

With v_{ram}=6 mm/s and μ=12 Pa s, five different grid sizes (2.0 mm, 1.0 mm, 0.4 mm, 0.3 mm and 0.2 mm) were used to determine if the solution was grid-independent. As shown in Fig. 4, the extrusion pressure of the ram by the mesh sizes of 0.4 mm to 0.2 mm was the same, while the extrusion pressure by the mesh sizes of 2.0 mm and 1.0 mm was significantly different. The extrusion pressure varied by less than 0.3% when the mesh size was changed from 0.4 mm to 0.2 mm. Therefore, a mesh size of 0.4 mm was utilized in this study.

RESULTS AND DISCUSSION

1. Verification of Modeling

Fig. 5 depicts the pressure obtained from simulation and experiment under the same operating conditions. The experimental data matched the simulation results with a maximum error of not higher than 5%. Therefore, the CFD model can be expected to simulate the extrusion pressure in the following extrusion process simulations.

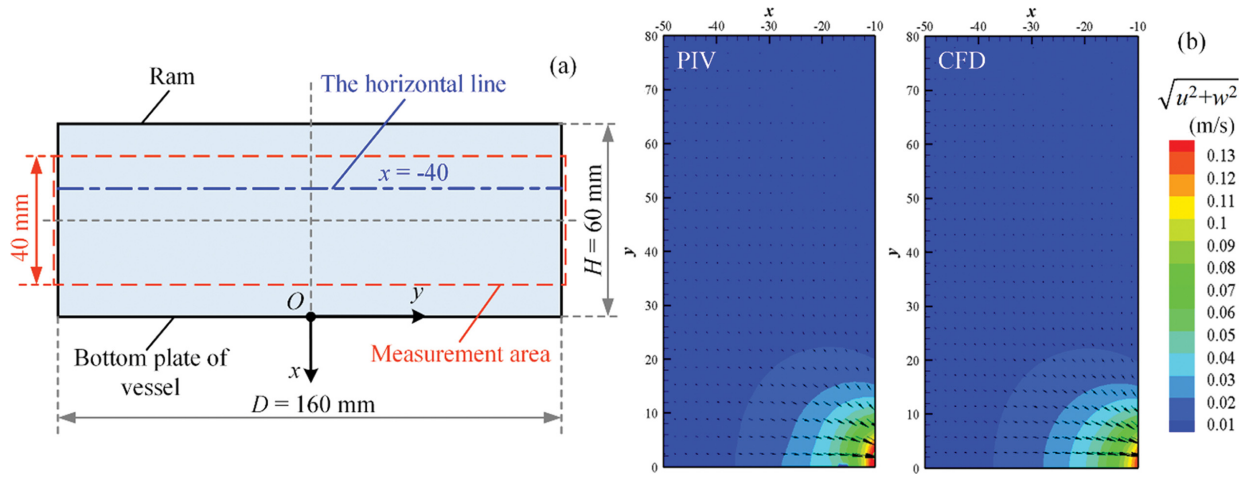

Fig. 6. (a) Schematic of measurement area; (b) Comparison of velocity contours and vectors obtained from experiments and simulations with v_{ram}=2 mm/s and μ=4 Pa s.

To qualitatively verify that the CFD model can accurately obtain velocity fields, the velocity contours and vectors obtained from experiments and simulations (when H=60 mm) are plotted in Fig. 6. The material of the ram and the bottom plate of the vessel is stainless steel. Therefore, to reduce the influence of the ram and the bottom plate of the vessel on the measurement of the flow field, the middle area between the ram and the bottom of the vessel was selected for velocity field measurement; the schematic of measurement area is shown in Fig. 6(a). As can be seen from Fig. 6(b), the simulation and experimental results are in good agreement. The CFD simulation results present the similar characteristics observed by the PIV experiment.

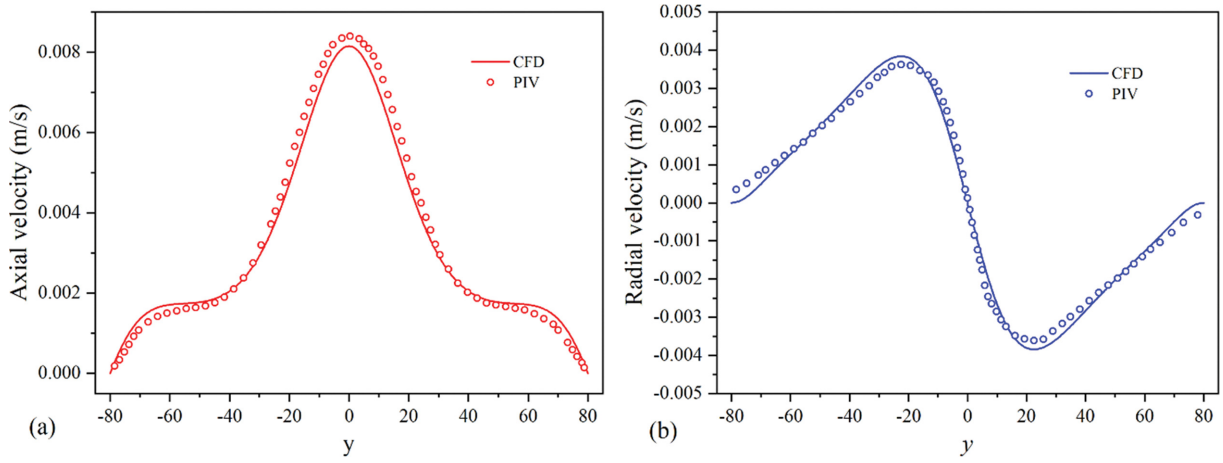

Fig. 7. Comparison of (a) axial velocity and (b) radial velocity between experiments and simulations (v_{ram}=2 mm/s, μ=4 Pa s) when H=60 mm (at x=−40 mm).

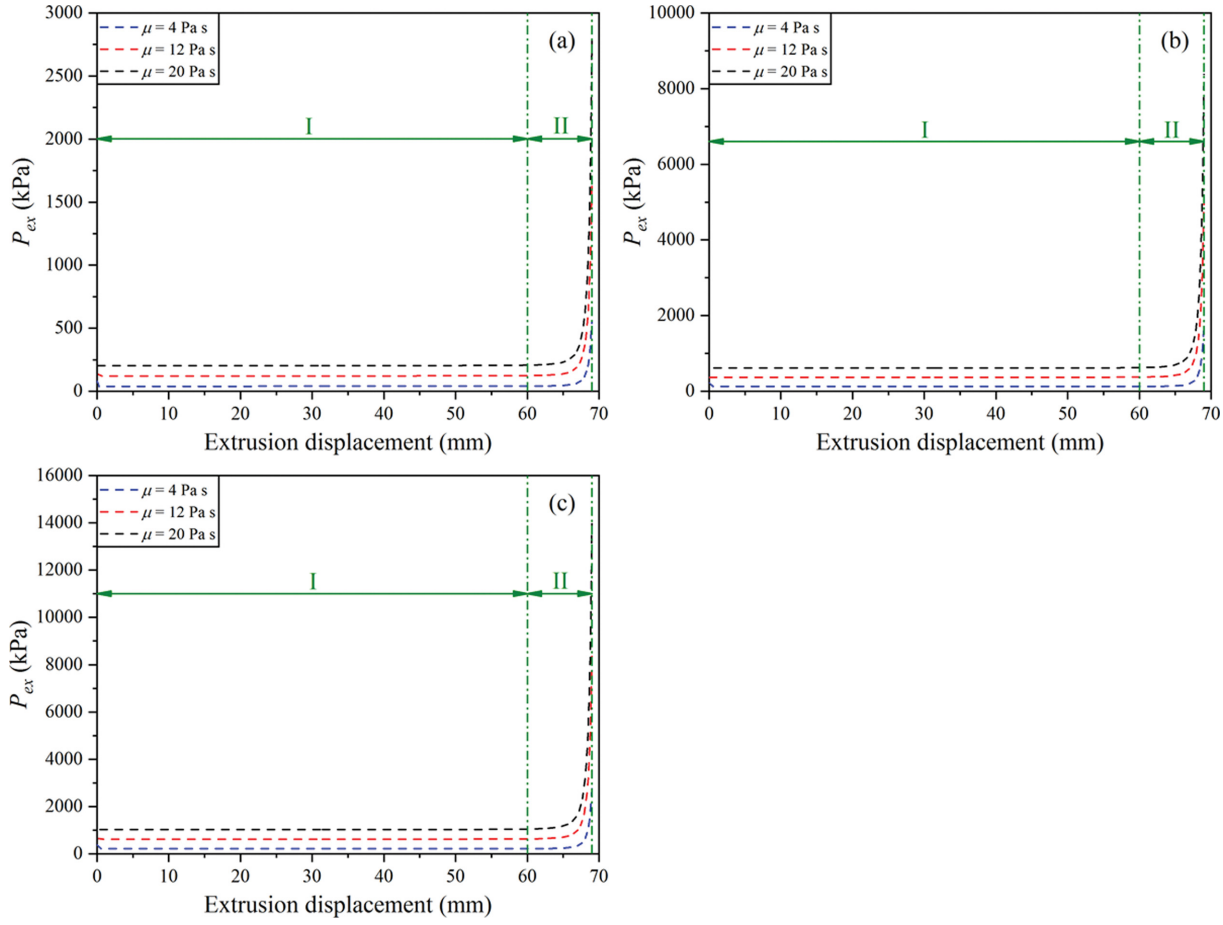

Fig. 8. Evolution of the extrusion pressure over extrusion displacement. (a) v_{ram}=2 mm/s, (b) v_{ram}=6 mm/s, (c) v_{ram}=10 mm/s.

To further quantitatively compare experimental and simulation results, Fig. 7 displays the comparison of axis velocity and radial velocity along the horizontal line (at x=−40 mm when H=60 mm) between experiment and simulation. For the axis velocity and radial velocity components, the average errors between the simulated and experimental results along the horizontal line at x=−40 mm are 9.5% and 10.3%, respectively. Therefore, the present CFD model is reliable enough to investigate the cylindrical extruder in this study.

2. Evolution of the Extrusion Pressure and its Mechanism

This study analyzes the evolution of the extrusion pressure during the 69 mm displacement of the ram (the ram runs from H=70 mm to H=1 mm) to understand the extrusion pressure P_{ex} variations during extrusion. The extrusion velocity is v_{ram}=2 mm/s, 6 mm/s and 10 mm/s, and the viscosity μ=4 Pa s, 12 Pa s and 20 Pa s, respectively.

Fig. 8 displays the evolution of the extrusion pressure over the extrusion displacement when the ram drives fluids of different viscosities μ at different extrusion velocities v_{ram}. The results indicate that the extrusion pressure remains relatively unchanged (change less than 2%), from the beginning of the movement of the ram to the extrusion displacement of 60 mm (that is, the ram runs from H=70 mm to H=10 mm). This indicates that in the initial stage, variation of H has almost no effect on the extrusion pressure. When H<10 mm (the extrusion displacement is greater than 60 mm), the extrusion pressure increases significantly with the decreasing H. In the final stage, the extrusion pressure rapidly increases to 12.97 times-14.11 times of the initial extrusion pressure. A similar phenomenon has been reported by Liu et al. [34], who analyzed the effect of different extrusion velocities on the extrusion pressure while extruding an aqueous ceramic paste. However, the pressure distribution near the wall of the ram during the extrusion process and the mechanism of the variation of the extrusion pressure needs further research.

Fig. 9 shows the variation of pressure distribution near the wall of the ram with different H during the extrusion process at v_{ram}= 6 mm/s and μ=12 Pa s. As depicted in Fig. 9, when the ram moves from H=70 mm to H=20 mm, the variation of H does not change the magnitude and distribution of pressure. Furthermore, the pressure near the wall of the ram is unchanged along the radial direction. Fig. 10 shows the contours of static pressure in the same extrusion process with H=60 mm, 40 mm and 20 mm, respectively. The movement of the ram does not modify the pressure field of the fluid domain in the extruder in this process. The maximum static pressure is 377 kPa when H changes from 60 mm to 20 mm.

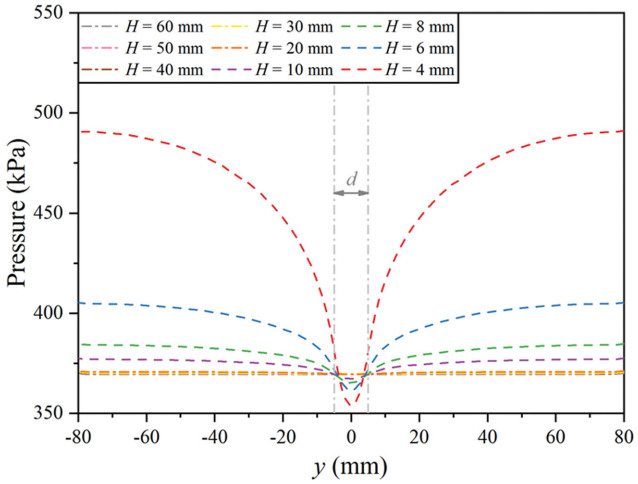

Fig. 9. The pressure distribution near the ram wall at v_{ram}=6 mm/s and μ=12 Pa s with different H.

However, the pressure distribution near the wall of the ram becomes non-uniform when H is less than 10 mm. As shown in Fig. 9, the pressure at the edge of the ram is the largest and gradually decreases from the edge to the center. The pressure reaches the minimum at the center of the ram. Furthermore, as H is decreased, the pressure at the edge increases while the pressure at the center decreases. Meanwhile, as shown in Fig. 11, the maximum static pressure rapidly increases from 378 kPa to 491 kPa as H decreases from 10 mm to 4 mm.

Although the pressure distribution near the wall of the ram when H=10 mm is not consistent with that when H≥20 mm, the maximum static pressure of 378 kPa when H=10 mm is nearly the same as 377 kPa when H≥20 mm. The difference in the extrusion pressure P_{ex} between H=10 mm and H≥20 mm is less than 1.8%. In this study, the extrusion process with nearly no change in the extrusion pressure, that is, when the extrusion stage H≥10 mm, is considered as stage I, and H<10 mm of the extrusion process is considered as stage II.

The fluid flow field exerts a great influence on the extrusion pressure during the extrusion process because velocity and pressure are interrelated, and investigating the fluid velocity distribution in

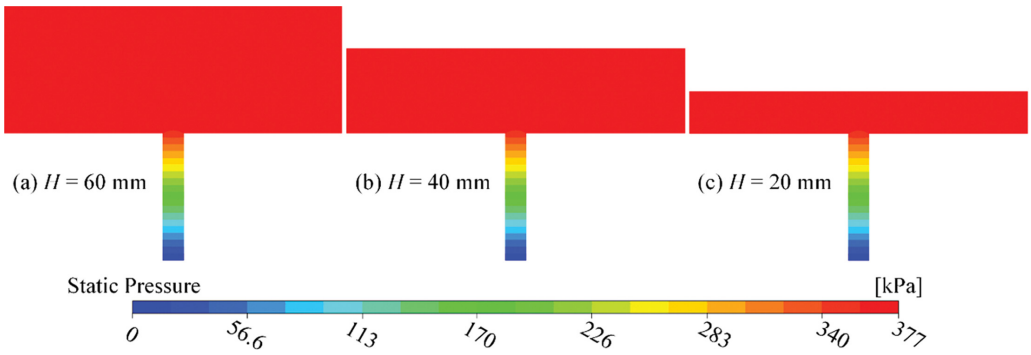

Fig. 10. Contours of static pressure in the case of v_{ram}=6 mm/s and μ=12 Pa s. (a) H=60 mm, (b) H=40 mm and (c) H=20 mm.

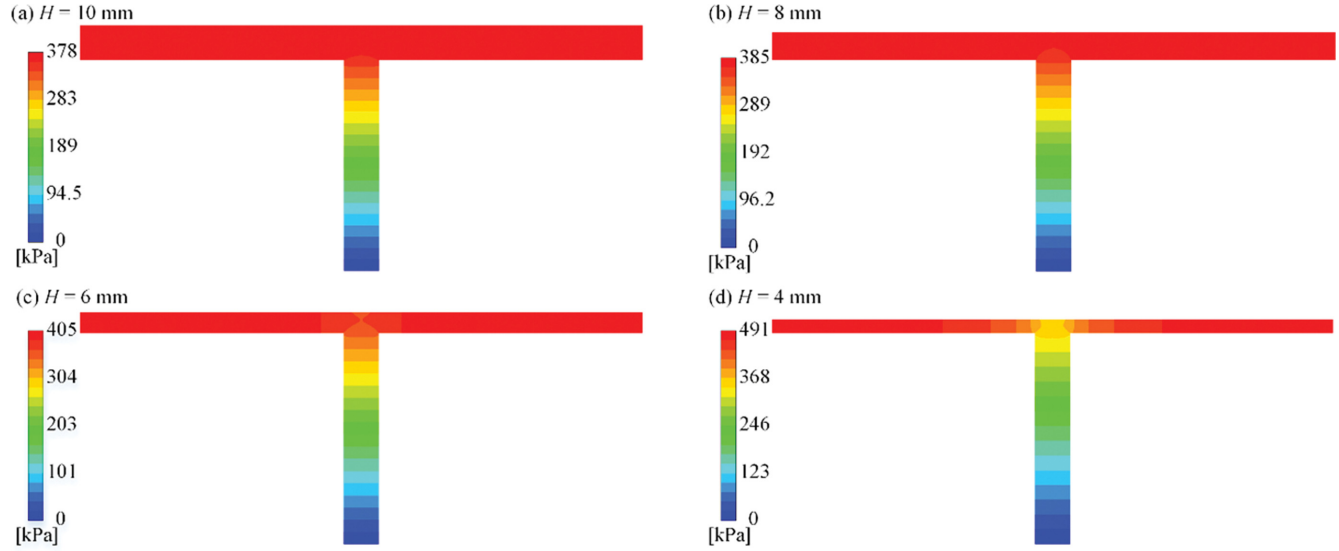

Fig. 11. Contours of static pressure in the case of v_{ram}=6 mm/s and μ=12 Pa s. (a) H=10 mm, (b) H=8 mm, (c) H=6 mm and (d) H=4 mm.

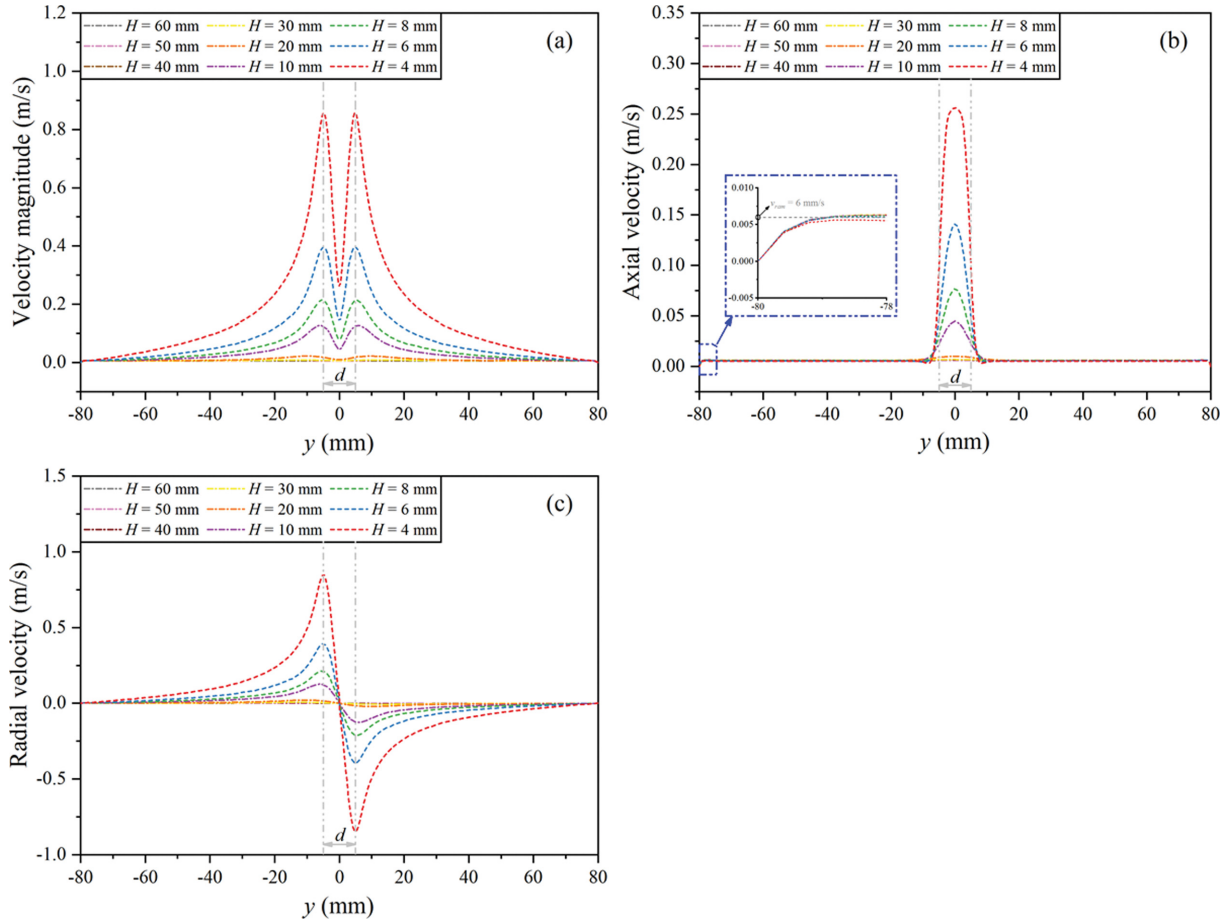

Fig. 12. The distribution of (a) velocity magnitude, (b) axial velocity, (c) radial velocity at 1 mm below the ram with different H at v_{ram}= 6 mm/s and μ=12 Pa s.

the extruder can enhance our understanding of the extrusion process of highly viscous fluids [35-37]. Fig. 12 and Fig. 13 show the distribution of velocity magnitude, axial velocity, and radial velocity at 1 mm below the ram and 1 mm above the bottom of the vessel with varied H, respectively.

During extrusion, the velocity components involved are axial

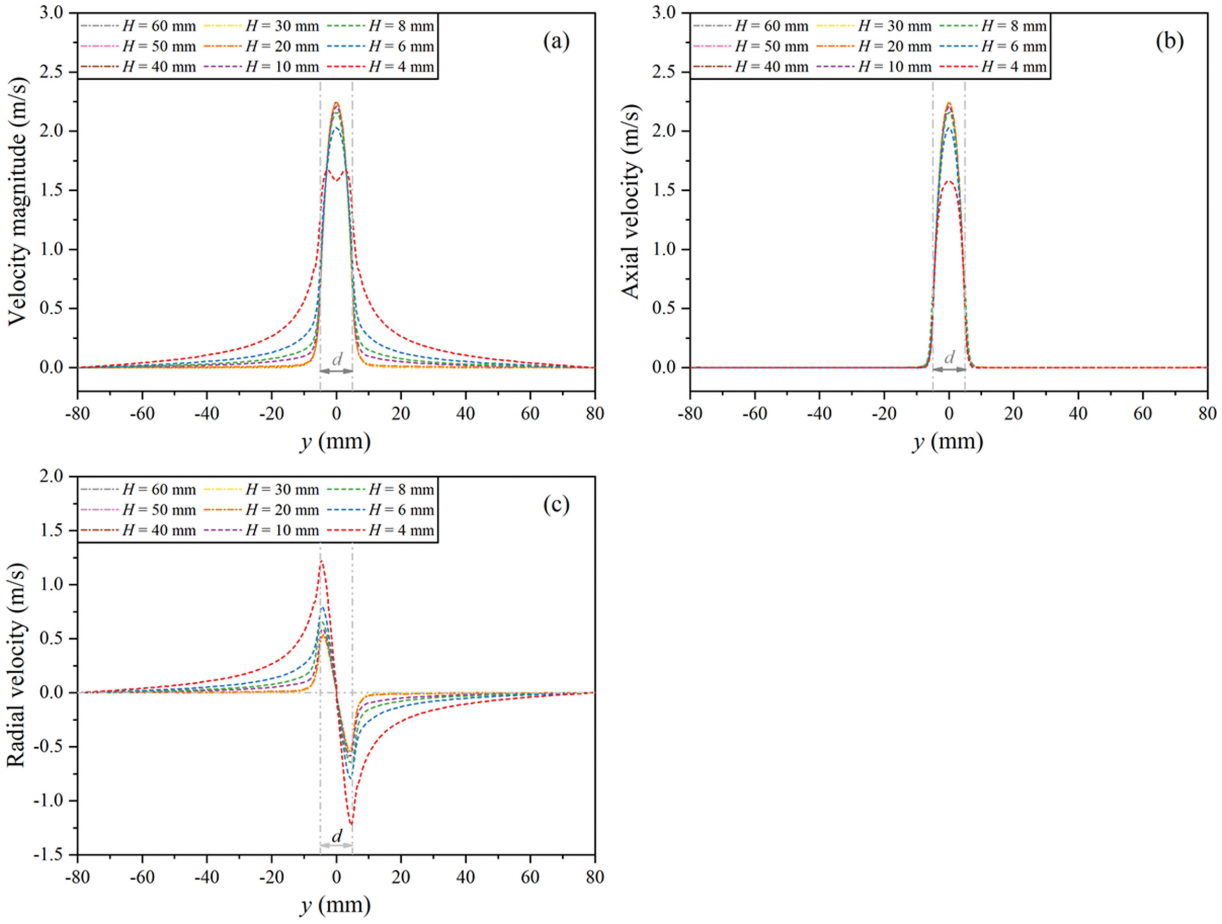

Fig. 13. The distribution of (a) velocity magnitude, (b) axial velocity, (c) radial velocity at 1 mm above the bottom of vessel with different H at v_{ram}=6 mm/s and μ=12 Pa s.

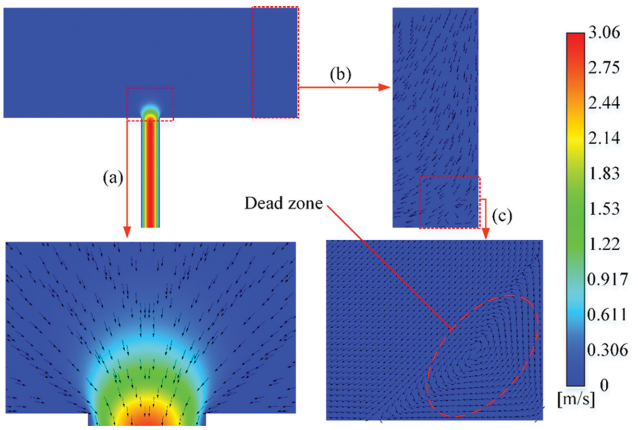

Fig. 14. Contours and vectors of velocity magnitude in the case of v_{ram}=6 mm/s and μ=12 Pa s with H=60 mm.

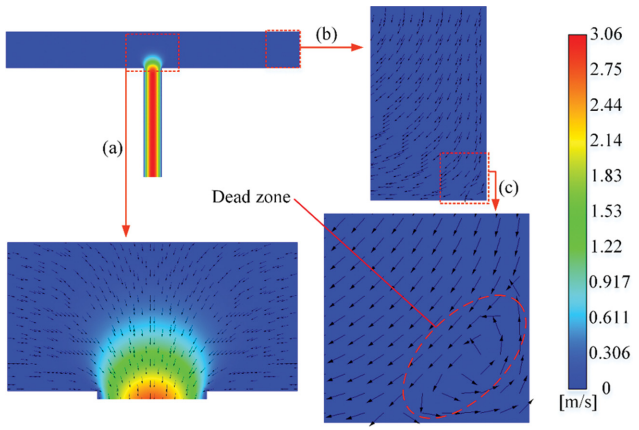

Fig. 15. Contours and vectors of velocity magnitude in the case of v_{ram}=6 mm/s and μ=12 Pa s with H=20 mm.

velocity and radial velocity. The axial velocity indicates that fluid flows along the extrusion direction, and the radial velocity implies that fluid flows perpendicular to the extrusion direction.

From Fig. 12, it is evident that when H≥10 mm, the velocity magnitude and distribution at 1 mm below the ram at different positions are very close to each other. As shown in Fig. 13, when the ram moves to different positions, the velocity magnitude and distribution at 1 mm above the bottom of the vessel hardly change when H≥10 mm. Fig. 14 and Fig. 15 display the contours and vectors of velocity magnitude at v_{ram}=6 mm/s and μ=12 Pa s with H=60 mm and 20 mm, respectively. Fig. 14 and Fig. 15 indicate that the velocity contours and vectors near the ram of H=60 mm and

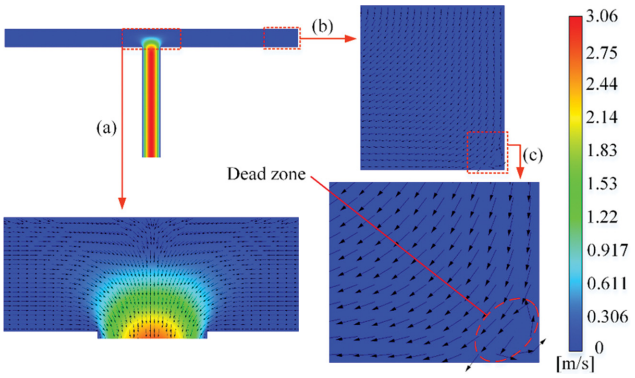

Fig. 16. Contours and vectors of velocity magnitude in the case of v_{ram}=6 mm/s and μ=12 Pa s with H=10 mm.

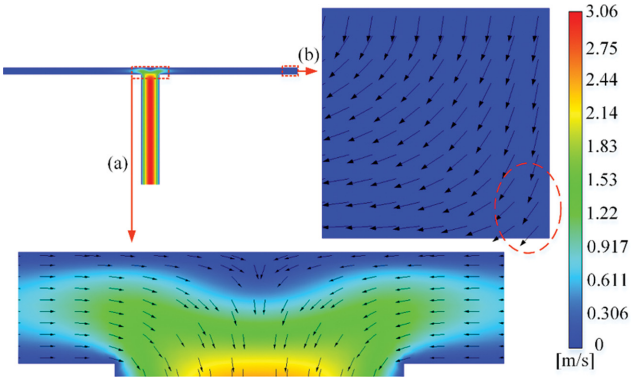

Fig. 17. Contours and vectors of velocity magnitude in the case of v_{ram}=6 mm/s and μ=12 Pa s with H=4 mm.

20 mm are very similar. This explains the phenomenon described in Fig. 8, Fig. 9 and Fig. 10, where the pressure distribution near the ram wall hardly changes as the ram moves to different positions when H≥10 mm. Note that during this process, the fluid velocity near the wall around the bottom of the vessel is almost zero (see Fig. 13), which when combined with Figs. 14(c) and 15(c), implies the existence of a static zone exists near the wall around the bottom of the vessel.

When H<10 mm, variation in the position of the ram causes significant changes in the velocity magnitude and distribution at 1 mm below the ram and 1 mm above the bottom of the vessel, as shown in Fig. 12 and Fig. 13. On comparing the results in Fig. 9, the corresponding changes in the position of the ram lead to variations in the fluid velocity magnitude and distribution, finally resulting in pressure distribution changes when H<10 mm. On comparing Figs. 14-17, it is observed that the dead zone near the wall around the bottom of the vessel decreases as H decreases. Once H<10 mm, the static zone becomes very small and almost disappears because, as the ram continues to extrude the liquid, the fluid velocity in the dead zone gradually increases (as shown in Fig. 13(a) and (c)), suggesting that the ram drives the fluid in the static zone to flow to the center of the vessel (as presented in Fig. 16 and Fig. 17). Besides, as reflected in Fig. 12, compared with stage I, the magnitude of fluid velocity near the ram increases significantly during this process. Consequently, at stage II, the extrusion pressure becomes larger than H≥10 mm.

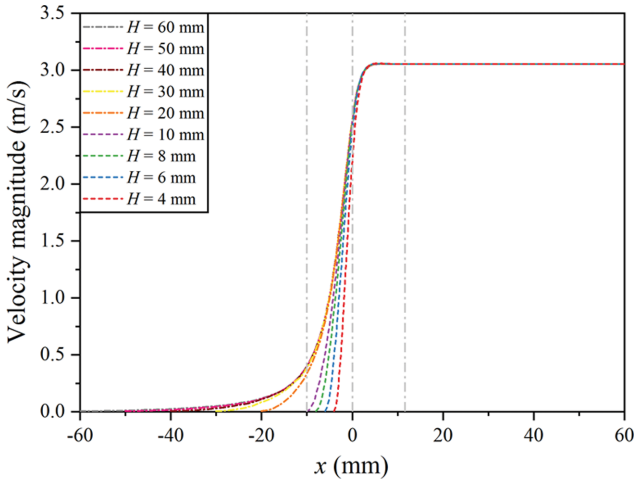

Fig. 18. Velocity magnitude along the centerline of the extruder with different H in the case of v_{ram}=6 mm/s and μ=12 Pa s.

Fig. 18 shows the velocity magnitude along the centerline of the extruder at v_{ram}=6 mm/s and μ=12 Pa s with different H. It is observed from Fig. 18 that when H≥10 mm, initially, the velocity increases gradually, which increases rapidly on approaching the bottom of the vessel. The velocity reaches its maximum value in die land and remains constant. When H<10 mm, the centerline velocity increases rapidly and finally has the same distribution as when H≥10 mm. This occurs because when the extrusion velocity is constant, the volume of fluid entering the die entrance per unit time is the same due to the conservation of volume. Finally, the ram at varying H forces the fluid velocity distribution in the die land to be uniform. Eventually, the velocity magnitude contours of die land and the maximum velocity shown in Fig. 14, Fig. 15, Fig. 16 and Fig. 17 are consistent.

For the quantitative assessment of the impact of H on the extrusion pressure, the critical height (H_c) is defined. When H≥H_c (at stage I), the variation of H has a negligible effect on the liquid flow field during the extrusion process; the extrusion pressure, P_{ex}, hardly changes (deviation less than 2%). Therefore, the influence of H can be ignored when predicting the extrusion pressure (P_{ex}) at stage I (H≥H_c). Worth noting is that H_c is the maximum value of H at stage II. In this study, the critical height H_c=10 mm is independent of the extrusion velocity and fluid viscosity.

3. Effect of Extrusion Velocity on the Extrusion Pressure P_{ex} at Stage I

Fig. 19 illustrates the extrusion pressure (P_{ex}) at stage I for four different fluid viscosities (μ=4 Pa s, 9 Pa s, 15 Pa s, and 20 Pa s) at different extrusion velocities (v_{ram}). As observed from Fig. 19, the extrusion pressure gradually increases with the increase of extrusion velocity, which can be explained by the change in the volume-averaged shear rate ($\dot{\gamma}$) and shear stress (τ) of the fluid domain. The extrusion velocity v_{ram} affects the fluid flow velocity, thereby having a direct impact on the volume-averaged shear rate $\dot{\gamma}$. Fig. 20(a) shows the volume-averaged shear rate $\dot{\gamma}$ of the whole fluid domain. For a given viscosity μ, the volume-averaged shear rate $\dot{\gamma}$ increases from 1.20±0.01 to 5.96±0.04 1/s as v_{ram} increases from 2

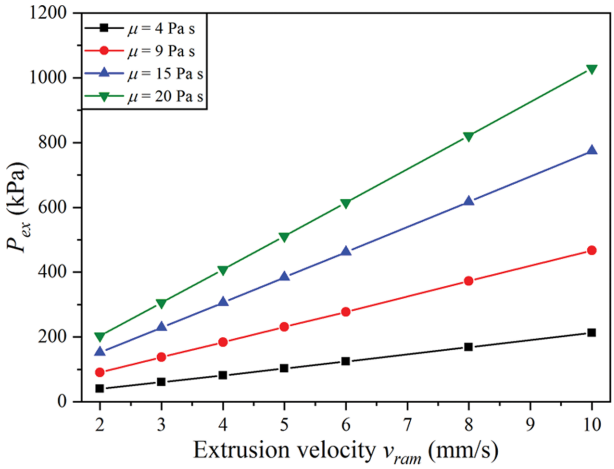

Fig. 19. Effect of extrusion velocity on the extrusion pressure.

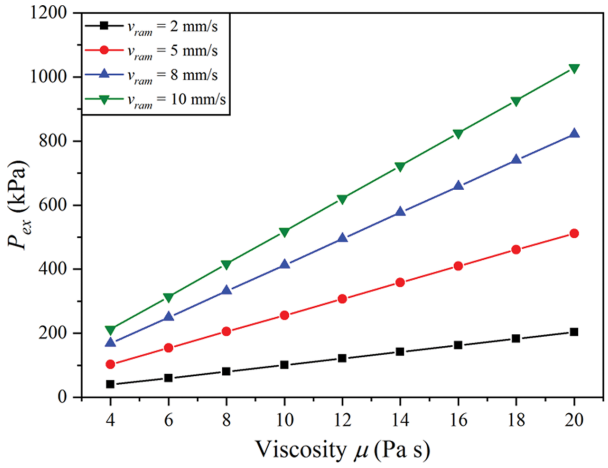

Fig. 21. Effect of viscosity of fluids on extrusion pressure.

to 10 mm/s. The volume-averaged shear stress τ increases by 398.1± 2.1% as shown in Fig. 20(b). This implies that the flow resistance will increase; therefore, the ram needs to provide greater force to drive the fluid flow.

4. Effect of Viscosity on the Extrusion Pressure P_{ex} at Stage I

Fig. 21 depicts the extrusion pressure (P_{ex}) at stage I for the four different extrusion velocities (v_{ram}=2 mm/s, 5 mm/s, 8 mm/s, and 10 mm/s) with different viscosities μ of fluids. As observed in Fig. 21, the effect of viscosity on the extrusion pressure is similar to that of extrusion velocity. The extrusion pressure analyses for nine different viscosities and extruding at four distinct extrusion velocities in Fig. 21 indicate that a 400% increase in viscosity (from 4 to 20 Pa s) causes a 413%, 397%, 389%, and 385% increase in the extrusion pressure for extrusion velocity at 2 mm/s, 5 mm/s, 8 mm/s, and 10 mm/s, respectively. This is because, at a fixed extrusion velocity, as viscosity increases, the volume-averaged shear stress τ of the fluid domain gradually increases (see Fig. 22(b)), resulting in an increase in flow resistance as the viscous shear force increases [38]. Therefore, the extrusion pressure of the ram increases to provide a constant extrusion velocity with the increasing viscosity. Furthermore, in comparison with Fig. 20(a) and Fig. 22(a), an increase in viscosity induces a negligible change in the volume-averaged shear rate $\dot{\gamma}$ unlike the effect of extrusion velocity.

5. Correlation Equation for the Extrusion Pressure P_{ex}

N_p and Re_p can be calculated, based on Eq. (9) and Eq. (10), respectively. Fig. 23 represents the pressure number N_p as a function of the pressure-related Reynolds number Re_p. All data points can perfectly fit onto Eq. (13) with an R^2 value of 0.9997.

$$\mathrm{Ln}(N_p) = -\mathrm{Ln}(Re_p) + 5.29853 \tag{13}$$

According to Eqs. (9), (10) and (13), the extrusion pressure (P_{ex}) at stage I can be calculated:

$$P_{exI} = 200\frac{\mu v_{ram} D^2}{d^3} \quad \text{(at stage I)} \tag{14}$$

The reliability of Eq. (13) is validated by the simulated results, as shown in Fig. 24. It can be seen that the predicted and simulated results are in good agreement with v_{ram}=2-10 mm/s and μ=4-20 Pa s, recording less than 3.0% errors. This comparison provides evidence that Eq. (14) can be used to predict the extrusion pressure (P_{ex}) at stage I of cylindrical extruders in industrial applications.

According to the above analysis, an extrusion pressure index at

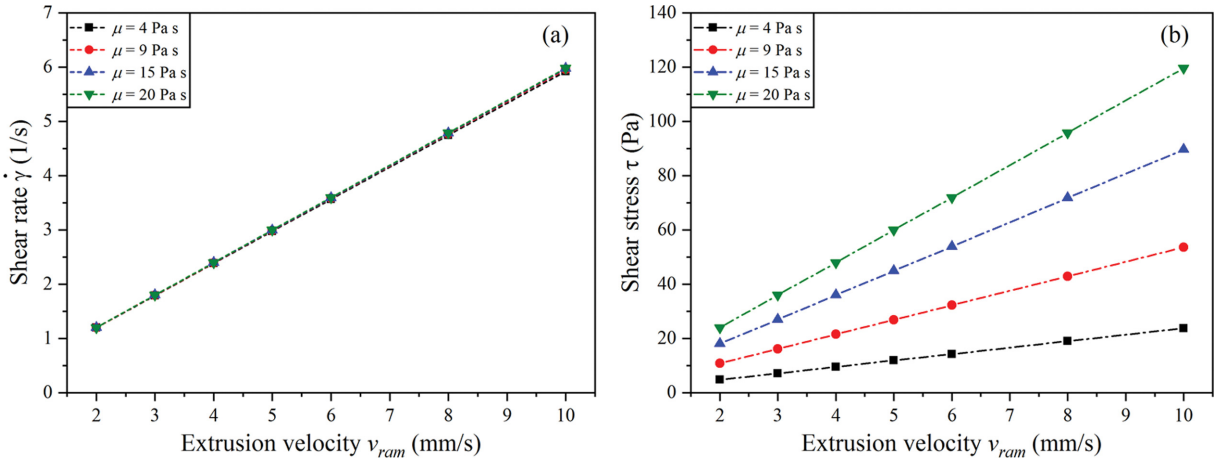

Fig. 20. The variation of volume-averaged (a) shear rate and (b) shear stress with different extrusion velocities.

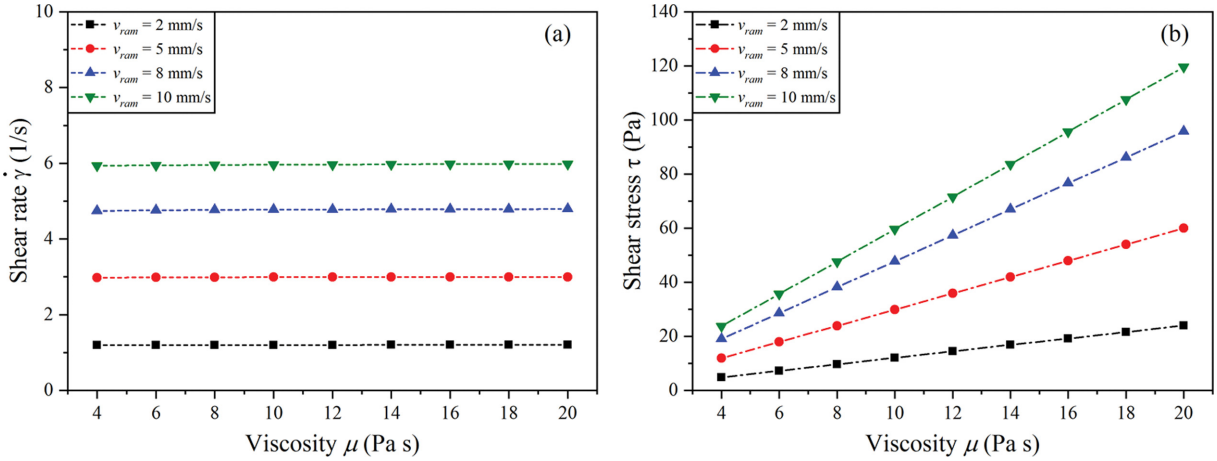

Fig. 22. The variation of volume-averaged (a) shear rate and (b) shear stress with different viscosity.

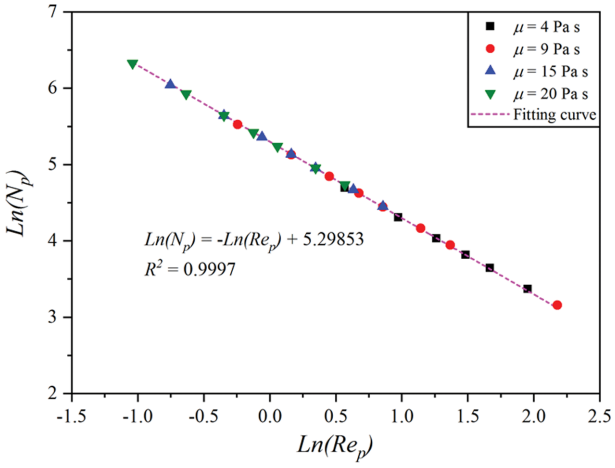

Fig. 23. Relationship between the pressure number N_p and pressure-related Reynolds number Re_p.

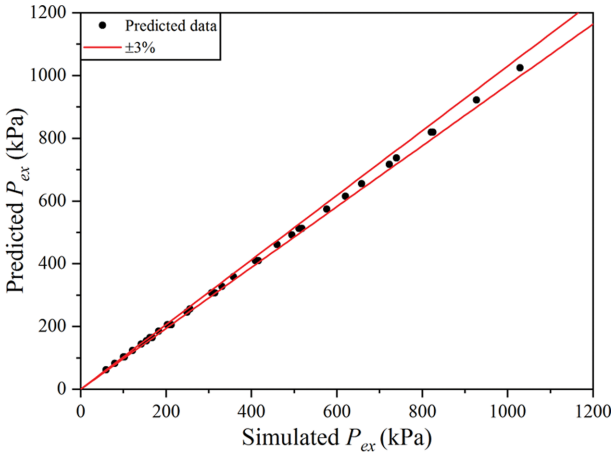

Fig. 24. Predicted P_{ex} versus simulated P_{ex} at stage I with v_{ram}=2-10 mm/s and μ=4-20 Pa s.

stage I K_{pI} is defined as:

$$K_{pI} = N_p \cdot Re_p \quad (15)$$

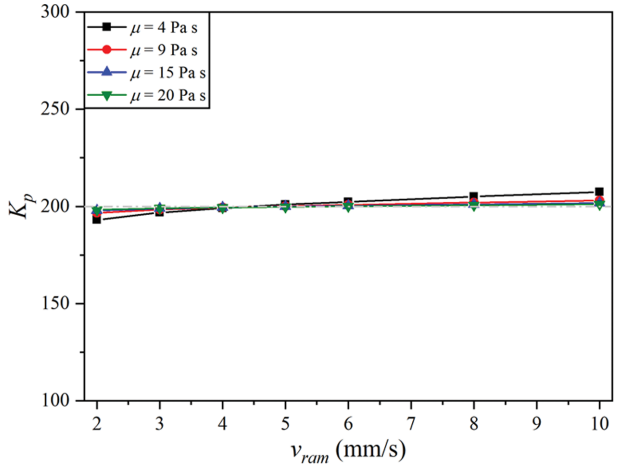

Fig. 25. The extrusion pressure index at stage I K_{pI} with v_{ram}=2-10 mm/s and μ=4-20 Pa s.

Fig. 25 shows the variation of K_{pI} with different v_{ram} and μ. The changes in extrusion velocity and fluid viscosity can hardly affect the extrusion pressure index K_{pI}. The maximum deviation of K_{pI} ((K_{pI}-avg(K_{pI}))/avg(K_{pI})) is 3.5% with v_{ram}=2-10 mm/s and μ=4-20 Pa s. Therefore, K_{pI} can be considered a dimensionless constant (which equal to 200 for the cylindrical extruder in this study) that accounts for the geometry effects of the extruder, such as the diameter of vessel D, the diameter of die land d, and the length of the die land L.

To study the relationship between the extrusion pressure (P_{ex}) at stage II and the distance between the ram and bottom of vessel (H), the relationship between P_{ex} and H is plotted in Fig. 26 based on the nine cases shown in Fig. 8. The following correlation is established by nonlinear fitting of these data (see Fig. 26) with an R^2 value of 0.9995:

$$\frac{P_{ex} - P_{exI}}{P_{exI}} = 0.023\left(\frac{H}{H_c}\right)^{-2.739} \quad (16)$$

where P_{exI} is the extrusion pressure at stage I. Defining an extrusion pressure index at stage II K_{pII} and a dimensionless parameter b, Eq. (16) can be written as:

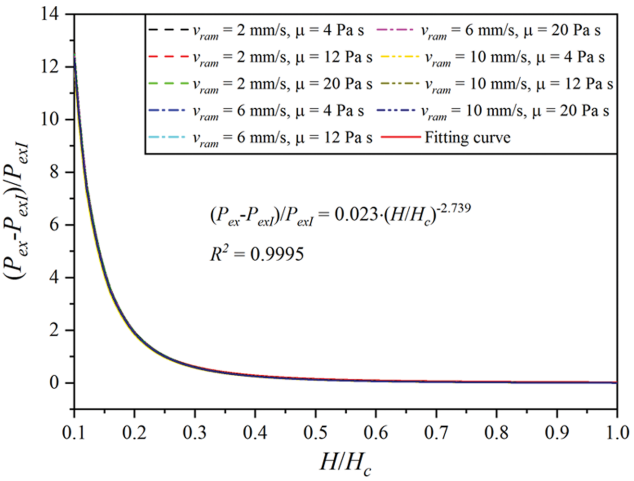

Fig. 26. The extrusion pressure P_{ex} at stage II with respect to H.

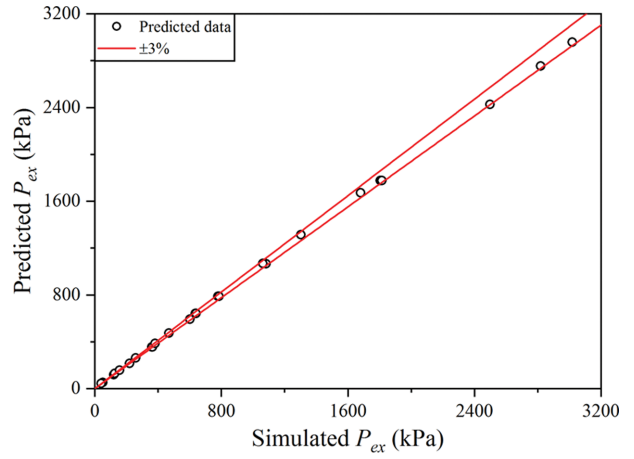

Fig. 27. Predicted P_{ex} versus simulated P_{ex} at stage II with H=1-10 mm, v_{ram}=2-10 mm/s and μ=4-20 Pa s.

$$P_{exII} = P_{exI} + P_{exI} K_{pII} \left(\frac{H}{H_c}\right)^b \quad \text{(at stage II)} \tag{17}$$

where K_{pII}=0.023, b=−2.739 and are independent of v_{ram} and μ.

The reliability of Eq. (17) is validated by the simulated results as shown in Fig. 27. It can be seen that the the predicted and simulated results agree well, with <3.0% errors. This comparison evidences that Eq. (17) can be used to predict the extrusion pressure at stage II of cylindrical extruder in industrial applications.

Based on the above research, the unit step function ε(t) is adopted. The unit step function, a non-smooth and piecewise constant function, [39] is defined as:

$$\varepsilon(t) = \begin{cases} 1, & t \geq 0 \\ 0, & t < 0 \end{cases} \tag{18}$$

In this case, the following function can be obtained:

$$\varepsilon\left(1-\frac{H}{H_c}\right) = \begin{cases} 1, & H \leq H_c \quad \text{(at stage II)} \\ 0, & H > H_c \quad \text{(at stage I)} \end{cases} \tag{19}$$

Therefore, by combining Eq. (14), Eq. (17) and Eq. (19), when extruding highly viscous fluids, the extrusion pressure P_{ex} of a cylindrical extruder with fixed geometry can be calculated by the following correlation:

$$P_{ex} = K_{pI} \frac{\mu v_{ram} D^2}{d^3} \left[1 + K_{pII} \left(\frac{H}{H_c}\right)^b \cdot \varepsilon\left(1-\frac{H}{H_c}\right)\right] \tag{20}$$

with v_{ram}=2-10 mm/s and μ=4-20 Pa s, in which K_{pI}, K_{pII} and b are dimensionless parameters that are independent of extrusion velocity (v_{ram}) and fluid viscosity (μ). The values of K_{pI}, K_{pII} and b in this study are 200, 0.023 and −2.739, respectively.

CONCLUSIONS

The evolution of the extrusion pressure and its mechanism when extruding highly viscous Newtonian fluids by a cylindrical extruder were explored by CFD simulations, and the effects of extrusion velocity and fluid viscosity on the extrusion pressure were further studied. Initially, an experimental setup for verifying the CFD model was established, and the pressure and velocity fields obtained by experiments were in good agreement with the simulation results.

The evolution of extrusion pressure and its mechanism were quantitatively and qualitatively investigated, which indicates a dead zone occurring at the bottom of the vessel. The dead zone divides the evolution of the extrusion pressure into two different development stages bounded by the critical height H_c. When the distance between ram and bottom of the vessel H>H_c, the velocity magnitude at 1 mm below the ram remained unchanged with the movement of the ram. Therefore, variation of H has a negligible effect on the extrusion pressure P_{ex}. While H<H_c, the movement of the ram drives the fluid in the dead zone to flow to the center of the vessel, the velocity magnitude at 1 mm below the ram increases significantly, P_{ex} increases exponentially with the decreases of H.

The effects of extrusion velocity v_{ram} and fluid viscosity μ on the extrusion pressure P_{ex} were evaluated. It was found that the increase of v_{ram} and μ leads to a linear increase in P_{ex} when H>H_c, respectively. Obviously, increasing extrusion velocity could improve the extrusion efficiency, but it would lead to a greater extrusion pressure. The balance of extrusion pressure and efficiency can only be achieved by selecting the appropriate v_{ram} based on μ. A correlation between P_{ex} with v_{ram} and μ was developed by introducing a pressure number N_p and a pressure-related Reynolds number Re_p. P_{ex} is linearly proportional to v_{ram} and μ, respectively, with v_{ram}=2-10 mm/s and μ=4-20 Pa s. When H>H_c, H has a negligible effect on the prediction model of P_{ex}, but P_{ex} follows by an exponentially increase with the decrease of H/H_c when H<H_c. This study provides a new perspective and method to predict the extrusion pressure of cylindrical extruders. This work will likely enhance our understanding of the variation in P_{ex} and the flow behavior in cylindrical extruders.

The present study specifically evaluates the extrusion pressure of a cylindrical extruder for Newtonian fluids. Further research is needed to investigate the extrusion pressure for non-Newtonian fluids.

NOMENCLATURE

b : exponent [dimensionless]

d : diameter of the die land [mm]
D : diameter of the vessel [mm]
$\vec{F}$: external body forces other than pressure [N/m^3]
$\vec{g}$: gravitational acceleration [m/s^2]
H : distance between ram and bottom of the vessel (liquid height) [mm]
H_c : the critical height (mm)
K_{pI} : the extrusion pressure index at stage I [dimensionless]
K_{pII} : the extrusion pressure index at stage II [dimensionless]
L : length of the die land [mm]
m : exponent for velocity-dependent yield stress [dimensionless]
n : exponent for velocity-dependent wall shear stress [dimensionless]
N_p : pressure number [dimensionless]
p : the fluid pressure [Pa]
P_{ex} : extrusion pressure [Pa]
P_{exI} : extrusion pressure at stage I [Pa]
P_{exII} : extrusion pressure at stage II [Pa]
Re_p : pressure-related number [dimensionless]
t : time [s]
$\vec{v}$: velocity vector [m/s]
v_{die} : fluid velocity in die land [mm/s]
v_{ram} : extrusion velocity [mm/s]

Greek Letters

α : velocity coefficient for yield stress [Pa/(m/s)^m]
β : wall slip shear rate coefficient [Pa/(m/s)^n]
$\dot{\gamma}$: volume-averaged shear rate of the fluid domain [1/s]
μ : viscosity [Pa s]
ρ : density [kg/m^3]
σ_0 : the yield stress [Pa]
τ : volume-averaged shear stress of the fluid domain [Pa]
τ_0 : wall slip yield stress [Pa]

Abbreviations

CFD : computational fluid dynamics
PIV : Particle Image Velocity

REFERENCES

1. S. Naumann, U. Schweiggert-Weisz, A. Martin, M. Schuster and P. Eisner, *Food Hydrocolloid.*, **111**, 106222 (2021).
2. N. Vitorino, M. J. Ribeiro, J. C. C. Abrantes, J. A. Labrincha and J. R. Frade, *Ceram. Int.*, **40**, 14543 (2014).
3. T. O. Althaus and E. J. Windhab, *Powder Technol.*, **211**, 10 (2011).
4. S. Mascia, M. J. Patel, S. L. Rough, P. J. Martin and D. I. Wilson, *Eur. J. Pharm. Sci.*, **29**, 22 (2006).
5. K. Prabha, P. Ghosh, S. Abdullah, R. M. Joseph, R. Krishnan, S. S. Rana and R. C. Pradhan, *Future Foods*, **3**, 100019 (2021).
6. Y. S. Lee and O. O. Park, *Korean J. Chem. Eng.*, **11**, 1 (1994).
7. R. A. Basterfield, C. J. Lawrence and M. J. Adams, *Chem. Eng. Sci.*, **60**, 2599 (2005).
8. H. Khelifi, A. Perrot, T. Lecompte, D. Rangeard and G. Ausias, *Powder Technol.*, **249**, 258 (2013).
9. M. Cortada-Garcia, W. H. Weheliye, V. Dore, L. Mazzei and P. Angeli, *Chem. Eng. Sci.*, **179**, 133 (2018).
10. G. Yang, A. Terzis, I. Zarikos, S. M. Hassanizadeh, B. Weigand and R. Helmig, *Chem. Eng. J.*, **370**, 444 (2019).
11. J. Jin and Y. Fan, *Korean J. Chem. Eng.*, **37**, 755 (2020).
12. A. Silva, F. J. G. Silva, R. D. S. G. Campilho and P. M. P. F. Neves, *J. Manuf. Processes*, **65**, 80 (2021).
13. H. Zhang, X. Zhao, X. Deng, M. A. Sutton, A. P. Reynolds, S. R. McNeill and X. Ke, *Int. J. Mech. Sci.*, **85**, 130 (2014).
14. M. P. Serdeczny, R. Comminal, M. T. Mollah, D. B. Pedersen and J. Spangenberg, *Additive Manuf.*, **36**, 101454 (2020).
15. C. Soanuch, K. Korkerd, J. Phupanit, R. Piemjaiswang, P. Piumsomboon and B. Chalermsinsuwan, *Korean J. Chem. Eng.*, **38**, 540 (2021).
16. P. Jay, A. Magnin and J. M. Piau, *J. Fluids Eng.*, **124**, 700 (2002).
17. Q. Liu, N. Zhang, W. Wei, X. Hu, Y. Tan, Y. Yu, Y. Deng, C. Bi, L. Zhang and H. Zhang, *J. Food Eng.*, **275**, 109861 (2020).
18. D. J. Ryan, M. J. H. Simmons and M. R. Baker, *Chem. Eng. Sci.*, **163**, 123 (2017).
19. D. J. Horrobin and R. M. Nedderman, *Chem. Eng. Sci.*, **53**, 3215 (1998).
20. T. Jiang, J. G. Munguia-Lopez, S. Flores-Torres, J. Kort-Mascort and J. M. Kinsella, *Appl. Phys. Rev.*, **6**, 11310 (2019).
21. M. J. Ribeiro, S. Blackburn, J. M. Ferreira and J. A. Labrincha, *J. Eur. Ceram. Soc.*, **26**, 817 (2006).
22. Y. Y. Li and J. Bridgwater, *Powder Technol.*, **108**, 65 (2000).
23. Z. Lin, T. Jiang, J. M. Kinsella, J. Shang and Z. Luo, *Mater. Lett.*, **303**, 130480 (2021).
24. J. J. Benbow, E. W. Oxley and J. Bridgwater, *Chem. Eng. Sci.*, **42**, 2151 (1987).
25. C. Bhattacharjee, *Korean J. Chem. Eng.*, **21**, 556 (2004).
26. K. Lachin, C. Turchiuli, V. Pistre, G. Cuvelier, S. Mezdour and F. Ducept, *Chem. Eng. Res. Des.*, **163**, 36 (2020).
27. C. André, J. F. Demeyre, C. Gatumel, H. Berthiaux and G. Delaplace, *Chem. Eng. J.*, **198-199**, 371 (2012).
28. M. Davarpanah, H. Shi, P. Nikrityuk and Z. Hashisho, *Chem. Eng. Res. Des.*, **173**, 289 (2021).
29. S. L. Rough, D. I. Wilson and J. Bridgwater, *Chem. Eng. Res. Des.*, **80**, 701 (2002).
30. K. E. Ryltseva, E. I. Borzenko and G. R. Shrager, *J. Non-Newton. Fluid*, **286**, 104445 (2020).
31. H. Bouras, Y. Haroun, R. Philippe, F. Augier and P. Fongarland, *Chem. Eng. Sci.*, **233**, 116378 (2021).
32. R. K. Connelly and J. L. Kokini, *J. Food Eng.*, **79**, 956 (2007).
33. E. Bumrungthaichaichan, *Korean J. Chem. Eng.*, **33**, 3050 (2016).
34. H. Liu, J. Liu, M. C. Leu, R. Landers and T. Huang, *Int. J. Adv. Manuf. Technol.*, **67**, 899 (2013).
35. Y. Sun, J. Yu, W. Wang, S. Yang, X. Hu and J. Feng, *Korean J. Chem. Eng.*, **37**, 743 (2020).
36. F. Keramat, A. Mirvakili, A. Shariati and M. R. Rahimpour, *Korean J. Chem. Eng.*, **38**, 2020 (2021).
37. S. I. Choi, J. P. Feng, H. S. Seo, Y. M. Jo and H. C. Lee, *Korean J. Chem. Eng.*, **35**, 2164 (2018).
38. W. Han and X. Chen, *Chem. Eng. Res. Des.*, **145**, 213 (2019).
39. S. Melzi, *Comput. Graphics*, **82**, 117 (2019).